Energy and Buildings 67 (2013) 322–333

Contents lists available at ScienceDirect

Energy and Buildings

journal homepage: www.elsevier.com/locate/enbuild

Performance assessment of a BIPV integrated with a layer of water-saturated MEPCM

C.J. Ho [a], Bor-Tyng Jou [a], Chi-Ming Lai [b,*], Chao-Yang Huang [c,d]

[a] Department of Mechanical Engineering, National Cheng Kung University, Tainan, Taiwan
[b] Department of Civil Engineering, National Cheng Kung University, Tainan, Taiwan
[c] Green Energy and Environment Research Laboratories, Industrial Technology Research Institute, Hsinchu, Taiwan
[d] Department of Mechanical Engineering, National Chiao Tung University, Hsinchu, Taiwan

ARTICLE INFO

Article history:
Received 10 December 2012
Received in revised form 14 June 2013
Accepted 18 August 2013

Keywords:
Photovoltaic (PV)
Building-integrated photovoltaic (BIPV)
Microencapsulated phase change material (MEPCM)
Thermal management

ABSTRACT

The use of a water-saturated microencapsulated phase change material (MEPCM) layer as a passive thermal management medium for a building-integrated photovoltaic (BIPV) was modeled by CFD numerical simulation to explore the effects of different MEPCM melting points and MEPCM layer thicknesses on the thermal and electrical performance. The well-designed BIPV can hopefully remain at a relatively low temperature during peak sunshine hours due to the absorption of latent heat during the phase change of the MEPCM layer, which reduces the decrease in electric generation efficiency caused by the increase in temperature due to solar radiation, thereby enhancing the electric generation efficiency. The results showed that a BIPV integrated with a MEPCM layer produced a significant improvement in the thermal and electrical performance compared to an untreated PV module. Under local summer climatic conditions, a melting point of 30 °C and a 3-cm-thick MEPCM (using paraffin as the core material) layer are recommended for the thermal management medium.

1. Introduction

1.1. From PV to BIPV

Building-integrated photovoltaic (BIPV) refers to an architectural design approach that combines photovoltaic (PV) panels with the building construction system. This combination allows BIPV to not only feature a power generation function but also to become part of the building facade. A reduction in the total energy consumed by the building can be achieved when BIPV is integrated with shading devices, daylighting, and illumination. Thus, BIPV transforms buildings from energy consumers into active power generators and is important to promote sustainable development in the building sector.

1.2. BIPV heat issues

Generally, the power output from a PV system is roughly proportional to the PV cell area and the solar irradiation on the PV cell surface. The power output is also affected by shading, cell temperature, dust on the PV surface, the sunlight incidence angle, and the irradiation spectral distribution. The PV cell temperature is associated with the generation efficiency of the solar irradiation energy that is converted to electricity. The nominal power of a PV module is tested under standardized testing conditions (AM1.5, 25 °C, 1000 W/m^2). However, in a normal environment, it is difficult to maintain a PV cell temperature of 25 °C because the cell is affected by ambient climate and heat transfer conditions. The efficiencies in a PV module decrease as the module temperature increases [1]. Therefore, whenever possible, it is necessary to enhance the heat dissipation of a PV module.

1.3. Application of PCM on BIPV heat dissipation

During the processes of melting or solidification, a PCM (phase change material) can effectively release or store a great amount of latent heat. The temperature of PCM can also be stably maintained during the latent heat transfer process. Therefore, in the application of energy storage and thermal environmental control, PCM is a very promising material choice.

The applications of PCM include thermal storage [2–4], integration with building materials [5–18] and usage in fireproof engineering. Comprehensive literature reviews on PCMs, thermophysical properties, long term stability, impregnation methods, current building applications and their thermal performance analyses, as well as numerical simulation of buildings with PCMs can be found in the review articles [19–22].

* Corresponding author. Tel.: +886 6 2757575x63136; fax: +886 6 2090569.
E-mail addresses: lily.lcm@msa.hinet.net, cmlai@mail.ncku.edu.tw (C.-M. Lai).

0378-7788/$ – see front matter © 2013 Elsevier B.V. All rights reserved.
http://dx.doi.org/10.1016/j.enbuild.2013.08.035

Nomenclature

A_p	capsule surface area
c, C_p	specific heat (J/kg K)
C_F	Forchheimer coefficient
d_p	particle diameter
E	electricity
$\dot{E}$	electric power output per unit cell area (W/m^2)
g	gravitational acceleration (m/s^2)
G_s	incident solar irradiation (W/m^2)
$G_{s,o}$	maximum incident solar irradiation (W/m^2)
h	heat convection coefficient (W/m^2 K)
H	height (m)
h_{LS}	latent heat (J/kg)
k	thermal conductivity coefficient (W/m K)
K	Ergun surface constant (m^2)
P	pressure (N/m^2)
q	heat transfer rate (W)
q''	heat flux (W/m^2)
Q	accumulated heat in a time period (J)
t	time (s)
T	temperature (°C)
u^+	x-direction velocity (m/s)
u	dimensionless x-direction velocity (m/s)
U	overall heat transfer coefficient (W/m^2 K)
$\forall$	capsule volume (m^3)
v^+	y-direction velocity (m/s)
v	dimensionless y-direction velocity (m/s)
W	width (m)
x	$=x^+/W$
y	$=y^+/H$

Greek letters

α	thermal diffusivity (m^2/s)
$\alpha_{r,pv}$	absorptivity of the PV
$\beta_{T,f}$	fluid expansion coefficient $\left(=-\frac{1}{\rho_{f,o}}\left(\frac{\partial \rho_f}{\partial T}\right)_{\varepsilon_i,T_c}\right)$
δ	thickness (m)
ϕ	porosity
η	efficiency
κ_{pv}	temperature dependent coefficient
μ	viscosity (N s/m^2)
ν	kinematic viscosity (m^2/s)
ρ	density (kg/m^3)
τ_t	delaying coefficient
ω	dimensionless vorticity
ω^+	vorticity
ξ	melt fraction
Δ	difference
Ψ	dimensionless streamline
Ψ^+	streamline

Subscript

0	time = 0
avg	average
Bottom	bottom
c	boundary point
day	accumulated value of the investigated day
f	fluid
Gd	lower glass part
Gs	solar irradiation
Gu	upper glass part
i	initial; inside
in	inward
Ld	lower boundary of the left partition plate
left	left
Lr	right-hand side boundary of the left partition plate
Lr_d	right lower boundary part of the left partition plate
Lr_u	right upper boundary part of the left partition plate
Lu	upper boundary of the left partition plate
m	mixed MEPCM-fluid
max	maximum
M; melt	melt
night	night
off	HVAC off
o	outer; reference
on	HVAC on
out	outward
p	MEPCM particle
pcm	phase change material
pt	partition plate
pv	photovoltaic cell
ref	reference
rise	sunrise
Rd	lower boundary of the right partition plate
RL	left-hand side boundary of the right partition plate
RL_u	left upper boundary part of the right partition plate
RL_d	left lower boundary part of the right partition plate
Right	right
Ru	upper boundary of the right partition plate
set	sunset
stored	stored
T	outdoor air temperature
Top	top
w	wind
x	x-axis
y	y-axis
∞	environment
∞,i	indoor
∞,o	outdoor

Superscript

−	average
+	dimensional

The existing literature on MEPCM-incorporated BIPV effectiveness on solar heat removal is still limited. The present study aims to explore the efficacy of using a layer of water-saturated MEPCM as a passive thermal management medium for a PV module under various daily operation conditions, via CFD numerical simulations.

2. Mathematical formulation and numerical method

2.1. Test cell

The test cell is illustrated in Fig. 1. The copper-colored block represents the container for the MEPCM, and the gray block represents the MEPCM layer. Gs(t) denotes the amount of solar radiation; δ_{pv} denotes the PV cell thickness, and H_{pt} denotes the height of the top and bottom frame walls of the MEPCM container. The height and thickness of the left and right frame wall are denoted by H_{pt} and W_{pt}, respectively, and W and H denote the thickness and height of the MEPCM layer, respectively.

The resulting transient conjugate heat transfer processes of conduction across the PV layer, as well as buoyancy-driven water convection in the porous layer packed with MEPCM particles can then be modeled by invoking the following assumptions:

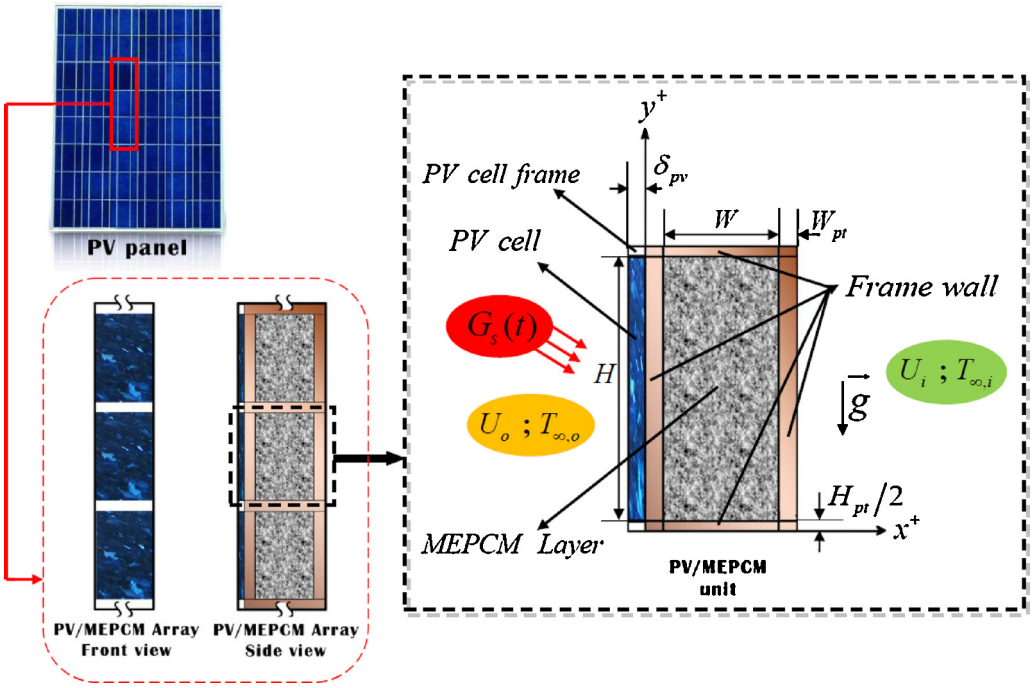

Fig. 1. Schematic of heat transfer in a PV/MEPCM module. The PV/MEPCM cell.

(a) Because the temperature gradient along the thickness δ_{pv} of the PV cell is negligibly small, the conduction is one-dimensional and takes place along its length.
(b) The thermal properties of the PV cell are isotropic and constant.
(c) The time-dependent solar irradiation onto the outer surface of the PV cell is uniform at $G_s(t)$.
(d) The outer surface of the PV cell has an effective absorptivity of $\alpha_{r,\,pv}$.
(e) The rectangular MEPCM layer is treated as a water-filled isotropic and homogenous porous medium with a porosity of ϕ_f.
(f) The MEPCM particles are spheres of uniform diameter d_p^+ in local thermal equilibrium with the fluid, except during the solid-liquid phase change process.
(g) The thermophysical properties of the fluid and the MEPCM particles are constant except for the density variation for the buoyancy force, which is treated using the Boussinesq approximation.

2.2. Dimensional mathematical model

2.2.1. Photovoltaic cell energy balance

The PV cell energy balance consists of a convection term, a solar irradiation term, and a term for the heat flux through the back of the cell. Two cells are shown in Fig. 2: a cell without a MEPCM layer (which will be referred to as an untreated PV cell) and a cell with a MEPCM layer (which will be referred to as a PV/MEPCM cell). The heat flux exiting the untreated PV cell is equal to the convection through the back of the cell, whereas the heat flux exiting the PV/MEPCM cell is equal to the heat flux entering the MEPCM layer.

The energy balance can be written as follows:

$$\rho_{pv}c_{pv}\delta_{pv}\frac{\partial T_{pv}}{\partial t} = k_{pv}\delta_{pv}\frac{\partial^2 T_{pv}}{\partial y^{+2}} + \alpha_{r,pv}G_s - \dot{E}_{pv} - U_o(T_{pv} - T_{\infty,o}) - q''_{pv,in} \quad (1)$$

The electric power output $\dot{E}_{pv}$ per unit cell area is calculated using the following equation:

$$\dot{E}_{pv} = G_s\eta_{pv} \quad (2)$$

where the electrical efficiency exhibits the following dependence on the PV temperature:

$$\eta_{pv} = \eta_{pv,ref}\left[1 - \kappa_{pv}\left(T_{pv} - T_{pv,ref}\right)\right] \quad (3)$$

where $T_{pv,ref}$ is the solar cell reference temperature of 25 °C and κ_{pv} is a material-dependent temperature coefficient for the PV cell, which has a value of 4.5×10^{-3} (1/K) in this study.

In addition, a gap forms between the upper and lower solar cells during the packaging of the PV modules. It is assumed that the material in the gap has properties similar to those of glass and that there is no heat transfer along the height and the thickness, as illustrated by the Gu and Gd points in Fig. 3. The frame point calculations for the PV cell can be divided into calculations for the untreated PV cell and the PV/MEPCM cell:

(a) Untreated PV cell

$$\rho_c c_{p,c}\frac{\partial T_{c,i}}{\partial t} = q''_{c,in} - q''_{c,out} \quad (4a)$$

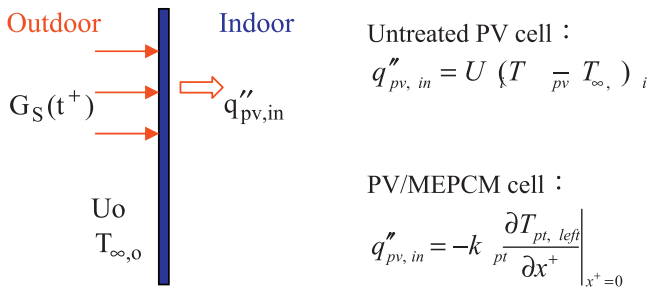

Fig. 2. PV cell energy balance.

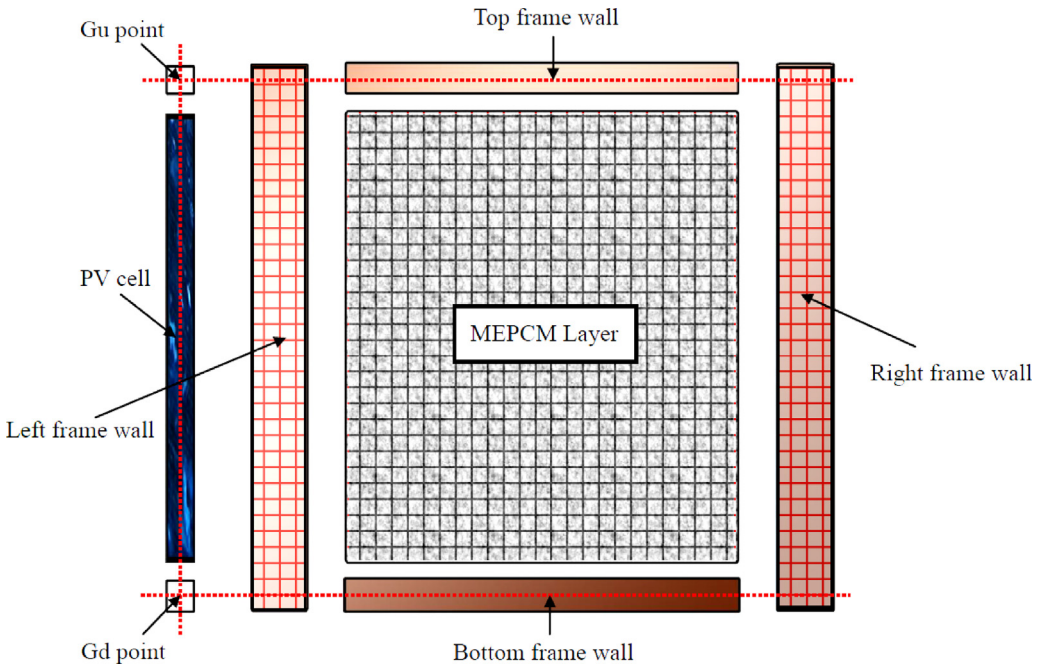

Fig. 3. Illustration of the computational domain (side view).

where

$$i=\begin{cases} Gu \Rightarrow q''_{c,in}=-k_{pv}\left.\dfrac{\partial T_{pv}}{\partial y^+}\right|_{y^+=H};\ q''_{c,out}=U_i(T_{c,i}-T_{\infty,i}) \\ Gd \Rightarrow q''_{c,in}=0;\ q''_{c,out}=-k_{pv}\left.\dfrac{\partial T_{pv}}{\partial y^+}\right|_{y^+=0}+U_i(T_{c,i}-T_{\infty,i}) \end{cases}.$$

(b) PV/MEPCM cell

$$\rho_c c_{p,c}\frac{\partial T_{c,i}}{\partial t}=q''_{c,in}-q''_{c,out} \tag{4b}$$

where

$$i=\begin{cases} Gu \Rightarrow q''_{c,in}=-k_{pv}\left.\dfrac{\partial T_{pv}}{\partial y^+}\right|_{y^+=H};\ q''_{c,out}=-k_{pt}\left.\dfrac{\partial T_{pt,Lu}}{\partial x^+}\right|_{x^+=0} \\ Gd \Rightarrow q''_{c,in}=0;\ q''_{c,out}=-k_{pv}\left.\dfrac{\partial T_{pv}}{\partial y^+}\right|_{y^+=0}-k_{pt}\left.\dfrac{\partial T_{pt,Ld}}{\partial x^+}\right|_{x^+=0} \end{cases}.$$

2.2.2. Mathematical equations

(a) Momentum equation for the MEPCM layer

Assuming only two-dimensional heat transfer inside the MEPCM layer, as illustrated in Fig. 3, the continuity equation can be expressed as follows:

$$\frac{\partial u^+}{\partial x^+}+\frac{\partial v^+}{\partial y^+}=0 \tag{5}$$

The momentum equation follows the Darcy–Brinkman–Forcheimer integrated model [23]. Using the Boussinesq approximation ($\Delta\rho_f \ll \Delta\rho_{f,0}$ and $\rho_f \approx \rho_{f,0}$) yields the following the x^+- and y^+-components of the momentum equations:

$$\beta_{T,f}=-\frac{1}{\rho_{f,0}}\left(\frac{\partial \rho_f}{\partial T}\right) \tag{6}$$

x^+-component of the momentum equation:

$$\rho_f\left[\phi_f{}^{-1}\frac{\partial u^+}{\partial t^+}+\phi_f{}^{-2}\left(u^+\times\nabla\right)u^+\right]=-\frac{\partial P^+}{\partial x^+}+\frac{\partial}{\partial x^+}\left(\mu_e\frac{\partial u^+}{\partial x^+}\right)+\frac{\partial}{\partial y^+}\left(\mu_e\frac{\partial u^+}{\partial y^+}\right)-\frac{\mu_f}{K}u^+-C_F K^{-0.5}\left|\vec{V}^+\right|u^+ \tag{7a}$$

y^+-component of the momentum equation:

$$\rho_f\left[\phi_f{}^{-1}\frac{\partial v^+}{\partial t}+\phi_f{}^{-2}\left(v^+\times\nabla\right)v^+\right]=-\frac{\partial P^+}{\partial y^+}+\frac{\partial}{\partial x^+}\left(\mu_e\frac{\partial v^+}{\partial x^+}\right)+\frac{\partial}{\partial y^+}\left(\mu_e\frac{\partial v^+}{\partial y^+}\right)-\frac{\mu_f}{K}v^+-g\rho_f\beta_{T,f}(T-T_{ref})-C_F K^{-0.5}\left|\vec{V}^+\right|v^+ \tag{7b}$$

where K is the Ergun equation coefficient, which is given by

$$K=\frac{d_p^2\phi_f^3}{150\left(1-\phi_f\right)^2} \tag{8}$$

where $\left|\vec{V}^+\right|=\sqrt{u^{+2}+v^{+2}}$ and C_F is the Forcheimer equation coefficient, which is set to 0.55. This value can be assumed to be constant as long as the porosity of the medium is between 0.4 and 0.6. The viscosity of the porous medium is denoted by μ_e, where, typically, $\mu_e=\mu_f$ for non-Darcy flow [23].

(b) Stream function and the vorticity equation

The stream function can be described by the following equation:

$$\frac{\partial^2\psi^+}{\partial x^{+2}}+\frac{\partial^2\psi^+}{\partial y^{+2}}=-\omega^+ \tag{9}$$

The vorticity equation is obtained by combining Eqs. (7a), (7b) and (9) to yield

$$\frac{1}{\phi_f}\frac{\partial \omega^+}{\partial t} + \frac{1}{\phi_f^2}\left(\frac{\partial(u^+\omega^+)}{\partial x^+} + \frac{\partial(v^+\omega^+)}{\partial y^+}\right) = \left(\frac{\tilde{\mu}}{\mu_f}\right)\frac{\nu_f}{\phi_f}\nabla^2\omega^+ + g\beta_{T,f}\frac{\partial T_m}{\partial x^+} - \frac{\nu_f}{K}\omega^+ - \frac{c_F}{\sqrt{K}}\left|\vec{u}\right|\omega^+ \quad (10)$$

(c) Energy balance

A heat transfer model for a rectangular container [24] is appropriated for the energy balance, which includes the melting rate for the phase change and the melting rate equations listed below:

$$\rho_m c_{p,m}\frac{\partial T_m}{\partial t} + \rho_f c_{p,f}\left(u^+\frac{\partial T_m}{\partial x^+} + v^+\frac{\partial T_m}{\partial y^+}\right) = \left[k_m\frac{\partial^2 T_m}{\partial x^{+2}} + k_m\frac{\partial^2 T_m}{\partial y^{+2}}\right] - \left(1-\phi_f\right)\rho_p h_{LS}\left(\frac{\partial \xi}{\partial t}\right) \quad (11)$$

The mixture density and the specific heat capacity of the mixture can be calculated as follows:

$$\rho_m = \phi_f\rho_f + (1-\phi_f)\rho_p \quad (12)$$

$$c_{p,m} = \frac{\phi_f\rho_f c_{p,f} + (1-\phi_f)\rho_p c_{p,p}}{\phi_f\rho_f + (1-\phi_f)\rho_p} \quad (13)$$

(d) Melting fraction equation

The relationship between the MEPCM temperature and the melted fraction can be described by the following equation:

$$\frac{\partial \xi}{\partial t} = \frac{A_p h_p}{\rho_p \forall_p h_{LS}}\left[(T_m - T_M) - \tau_t\frac{\partial T_m}{\partial t}\right] \quad (14)$$

The delay entry can be expressed as

$$\tau_t = \left[\frac{(\forall_p/A_p)^2}{\alpha_p}\right]\left(\frac{c_{p.m}}{c_{p,p}}\right) \quad (15)$$

(e) Energy balance for the container frame wall

Fig. 3 shows that the numerical computation block includes the PV cell, the frame points of the PV cell, the frame walls (top, bottom, left, and right) of the MEPCM container, and the MEPCM layer. Assuming that the top and bottom frame walls are symmetric, the gradient in the y-direction is zero. The energy balance between the top and bottom frame walls is given by:

$$\rho_{pt}c_{p,pt}H_{pt}\frac{\partial T_{pt,Top}}{\partial t} = k_{pt}H_{pt}\frac{\partial^2 T_{pt,Top}}{\partial x^{+2}} + q''_{pt,in};\ q''_{pt,in} = -k_m\left.\frac{\partial T_m}{\partial y^+}\right|_{y^+=H} \quad (16a)$$

$$\rho_{pt}c_{p,pt}H_{pt}\frac{\partial T_{pt,Bottom}}{\partial t} = k_{pt}H_{pt}\frac{\partial^2 T_{pt,Bottom}}{\partial x^{+2}} - q''_{pt,out};\ q''_{pt,out} = -k_m\left.\frac{\partial T_m}{\partial y^+}\right|_{y^+=0} \quad (16b)$$

Because the x-direction is the primary heat transfer direction, only heat conduction along the thickness of the left frame wall needs to be considered. However, the spacer grid on the boundary of the left frame wall must be considered separately to prevent non-convergence of the numerical scheme due to an energy imbalance between the contact surface of the frame wall and the MEPCM layer. The left boundary of the left frame wall directly contacts the PV cell so that the temperature of the left frame wall is equal to the temperature of PV cell. The corresponding energy balance for the left frame wall is given below.

(1) Points within the left frame wall ($0 < x^+ < W_{pt}$, $0 < y^+ < H$)

$$\rho_{pt}c_{p,pt}\frac{\partial T_{pt,Left}}{\partial t} = k_{pt}\left(\frac{\partial^2 T_{pt,Left}}{\partial x^{+2}} + \frac{\partial^2 T_{pt,Left}}{\partial y^{+2}}\right) \quad (17)$$

(2) Top and bottom boundaries of the left frame wall

$$\rho_{pt}c_{p,pt}H_{pt}\frac{\partial T_{pt,Lu}}{\partial t} = k_{pt}H_{pt}\frac{\partial^2 T_{pt,Lu}}{\partial x^{+2}} + q''_{pt,in};\ q''_{pt,in} = -k_{pt}\left.\frac{\partial T_{pt,Left}}{\partial y^+}\right|_{y^+=H};\quad 0 < x^+ < W_{pt},\ y^+ = H \quad (18a)$$

$$\rho_{pt}c_{p,pt}H_{pt}\frac{\partial T_{pt,Ld}}{\partial t} = k_{pt}H_{pt}\frac{\partial^2 T_{pt,Ld}}{\partial x^{+2}} - q''_{pt,out};\quad q''_{pt,out} = -k_{pt}\left.\frac{\partial T_{pt,Left}}{\partial y^+}\right|_{y^+=0};\quad 0 < x^+ < W_{pt},\ y^+ = 0 \quad (18b)$$

(3) Right boundary of the left frame wall ($x^+ = W_{pt}$; $0 < y^+ < H$)

$$\rho_{pt}c_{p,pt}W_{pt}\frac{\partial T_{pt,Lr}}{\partial t} = k_{pt}W_{pt}\frac{\partial^2 T_{pt,Lr}}{\partial y^{+2}} + q''_{pt,in} - q''_{pt,out} \quad (19)$$

where

$$q''_{pt,in} = -k_{pt}\left.\frac{\partial T_{pt,Left}}{\partial x^+}\right|_{x^+=W_{pt}};\quad q''_{pt,out} = -k_m\left.\frac{\partial T_m}{\partial x^+}\right|_{x^+=W_{pt}}$$

(4) Upper right ($x^+ = W_{pt}$, $y^+ = H$) and lower right boundary point ($x^+ = W_{pt}$, $y^+ = 0$) of the left frame wall

$$\rho_c c_{p,c}\frac{\partial T_{c,i}}{\partial t} = q''_{c,in} - q''_{c,out} \quad (20)$$

where

$$i = \begin{cases} Lr_u;\ q''_{c,in} = -k_{pt}\left.\frac{\partial T_{pt,Lu}}{\partial x^+}\right|_{x^+=W_{pt}} - k_{pt}\left.\frac{\partial T_{pt,Lr}}{\partial y^+}\right|_{y^+=H};\ q''_{c,out} = -k_{pt}\left.\frac{\partial T_{pt,Top}}{\partial x^+}\right|_{x^+=W_{pt}} \\ Lr_d;\ q''_{c,in} = -k_{pt}\left.\frac{\partial T_{pt,Ld}}{\partial x^+}\right|_{x^+=W_{pt}};\ q''_{c,out} = -k_{pt}\left.\frac{\partial T_{pt,Lr}}{\partial y^+}\right|_{y^+=0} - k_{pt}\left.\frac{\partial T_{pt,Bottom}}{\partial x^+}\right|_{x^+=W_{pt}} \end{cases}$$

The right frame wall is treated similarly to the left frame wall. The right boundary does not contact any other computational domain and does not need to be considered separately. The right boundary can be included in the internal points for the calculations as given below.

(1) Internal points of right frame wall ($W_{pt} + W < x^+ \le 2W_{pt} + W$, $0 < y^+ < H$)

$$\rho_{pt}c_{p,pt}\frac{\partial T_{pt,Right}}{\partial t} = k_{pt}\left(\frac{\partial^2 T_{pt,Right}}{\partial x^{+2}} + \frac{\partial^2 T_{pt,Right}}{\partial y^{+2}}\right) \quad (21)$$

(2) Top and bottom boundaries of right frame wall

$W_{pt} + W < x^+ \le 2W_{pt} + W,\ y^+ = H$:

$$\rho_{pt}c_{p,pt}H_{pt}\frac{\partial T_{pt,Ru}}{\partial t} = k_{pt}H_{pt}\frac{\partial^2 T_{pt,Ru}}{\partial x^{+2}} + q''_{pt,in};\ q''_{pt,in} = -k_{pt}\left.\frac{\partial T_{pt,Right}}{\partial y^+}\right|_{y^+=H} \quad (22a)$$

$W_{pt} + W < x^+ \le 2W_{pt} + W,\quad y^+ = 0$:

$$\rho_{pt}c_{p,pt}H_{pt}\frac{\partial T_{pt,Rd}}{\partial t} = k_{pt}H_{pt}\frac{\partial^2 T_{pt,Rd}}{\partial x^{+2}} - q''_{pt,out};\quad q''_{pt,out} = -k_{pt}\left.\frac{\partial T_{pt,Right}}{\partial y^+}\right|_{y^+=0} \quad (22b)$$

(3) Left boundary of the right frame wall ($x^+ = W_{pt} + W$; $0 < y^+ < H$)

$$\rho_{pt}c_{p,pt}W_{pt}\frac{\partial T_{pt,Rl}}{\partial t} = k_{pt}W_{pt}\frac{\partial^2 T_{pt,Rl}}{\partial y^{+2}} + q''_{pt,in} - q''_{pt,out} \quad (23)$$

where

$$q''_{pt,in} = -k_m \left.\frac{\partial T_m}{\partial x^+}\right|_{x^+=W_{pt}+W};\ q''_{pt,out} = -k_{pt} \left.\frac{\partial T_{pt,Right}}{\partial x^+}\right|_{x^+=W_{pt}+W}$$

(4) Upper left boundary point ($x^+ = W_{pt} + W$, $y^+ = H$) and lower left boundary point ($x^+ = W_{pt} + W$, $y^+ = 0$) of the right frame wall

$$\rho_c c_{p,c} \frac{\partial T_{c,i}}{\partial t} = q''_{c,in} - q''_{c,out} \tag{24}$$

where

$$i = \begin{cases} Rl_u;\ q''_{c,in} = -k_{pt} \left.\frac{\partial T_{pt,Top}}{\partial x^+}\right|_{x^+=W_{pt}+W} - k_{pt} \left.\frac{\partial T_{pt,Rl}}{\partial y^+}\right|_{y^+=H};\ q''_{c,out} = -k_{pt} \left.\frac{\partial T_{pt,Ru}}{\partial x^+}\right|_{x^+=W_{pt}+W} \\ Rl_d;\ q''_{c,in} = -k_{pt} \left.\frac{\partial T_{pt,Bottom}}{\partial x^+}\right|_{x^+=W_{pt}+W};\ q''_{c,out} = -k_{pt} \left.\frac{\partial T_{pt,Rl}}{\partial y^+}\right|_{y^+=0} - k_{pt} \left.\frac{\partial T_{pt,Rd}}{\partial x^+}\right|_{x^+=W_{pt}+W} \end{cases}$$

2.3. Initial conditions, boundary conditions, and environmental parameters

The initial temperatures of the PV cell, the container frame walls, and the MEPCM layer are assumed to be the same as the outdoor temperature. The boundary conditions for the MEPCM layers are set by assuming the same temperatures for the layers and the contacting frame walls.

2.3.1. Initial and boundary conditions for the PV cell

$t = 0$:

$$T_{pv}(y^+, t = 0) = T_{\infty,o} \tag{25}$$

$t > 0$:

$$y^+ = H : T_{pv} = T_{c,Gu} \tag{26a}$$

$$y^+ = 0 : T_{pv} = T_{c,Gd} \tag{26b}$$

2.3.2. Initial and boundary conditions for MEPCM layer

$t = 0$:

$$T_m(x^+, y^+, t=0) = T_{\infty,o};\quad \omega^+(x^+, y^+, t=0) = \psi^+(x^+, y^+, t=0) = 0 \tag{27}$$

$t > 0$:

$$x^+ = W_{pt} : \psi^+ = 0;\quad T_m = T_{pt,Left} \tag{28a}$$

$$x^+ = W_{pt} + W : \psi^+ = 0;\quad T_m = T_{pt,Right} \tag{28b}$$

$$y^+ = H : \psi^+ = 0;\quad T_m = T_{pt,Top} \tag{28c}$$

$$y^+ = 0 : \psi^+ = 0;\quad T_m = T_{pt,Bottom} \tag{28d}$$

2.3.3. Initial and boundary conditions for the MEPCM frame walls

$t = 0$:

$$T_{pt,Top}(x^+, t = 0) = T_{pt,Bottom}(x^+, t = 0) = T_{\infty,o} \tag{29a}$$

$$T_{pt,Left}(x^+, y^+, t = 0) = T_{pt,Right}(x^+, y^+, t = 0) = T_{\infty,o} \tag{29b}$$

$t > 0$:

(a) Boundary condition for the left frame wall

$$x^+ = 0,\ 0 < y^+ < H : T_{pt,Left} = T_{pv};\ q''_{pv,in} = -k_{pt} \left.\frac{\partial T_{pt,Left}}{\partial x^+}\right|_{x^+=0} \tag{30a}$$

$$x^+ = 0,\ y^+ = H : T_{pt,Left} = T_{c,Gu} \tag{30b}$$

$$x^+ = 0,\ y^+ = 0 : T_{pt,Left} = T_{c,Gd} \tag{30c}$$

(b) Boundary condition for the right frame wall

$$x^+ = 2W_{pt} + W,\ 0 \le y^+ \le H : -k_{pt} \frac{\partial T_{pt,Right}}{\partial x^+} = U_i \left(T_{pt,Right} - T_{\infty,i}\right) \tag{31}$$

(c) Boundary condition for the top frame wall and the bottom frame wall

$$x^+ = W_{pt} : T_{pt,Top} = T_{c,Lu};\ T_{pt,Bottom} = T_{c,Ld} \tag{32a}$$

$$x^+ = W_{pt} + W : T_{pt,Top} = T_{c,Ru};\ T_{pt,Bottom} = T_{c,Rd} \tag{32b}$$

2.3.4. Setting the environmental parameters

To describe the actual environmental conditions as closely as possible, solar radiation is considered to be a function of time. The level of solar radiation immediately before sunrise and immediately after sunset is zero. Immediately after sunrise, the radiation begins to increase until a maximum is reached, after which the radiation decreases until sunset. The solar radiation is modeled as follows:

$$G_s(t) = \begin{cases} 0, & 0 \le t < t_{rise,Gs} \\ G_{s,o} \sin[\frac{\pi(t - t_{rise,Gs})}{2(t_{\max,Gs} - t_{rise,Gs})}],\ t_{rise,Gs} \le t < t_{\max,Gs} \\ G_{s,o} \cos[\frac{\pi(t - t_{\max,Gs})}{2(t_{set,Gs} - t_{\max,Gs})}],\ t_{\max,Gs} \le t < t_{set,Gs} \\ 0, & t_{set,Gs} \le t \le 24 \end{cases} \tag{33}$$

where $t_{rise,Gs}$ is the time of sunrise; $t_{\max,Gs}$ is the time at which the solar radiation is at a maximum; and $t_{set,Gs}$ is the time of sunset.

Experimental measurements by our research group in 2011 demonstrated that there is no heat radiation to the outdoor air before sunrise and after sunset, and thus, the outdoor air temperature change is almost linear with time. Therefore, the actual outdoor temperature is approximated by a piece-wise function with four intervals, as follows:

$$T_{\infty,0}(t) = \begin{cases} T_{\infty,night} - t\left(\frac{T_{\infty,night} - T_{\infty,rise}}{t_{rise,T}}\right),\ 0 \le t < t_{rise,T} \\ T_{\infty,rise} + \left(T_{\infty,\max} - T_{\infty,rise}\right) \sin[\frac{\pi(t - t_{rise,T})}{2(t_{\max,T} - t_{rise,T})}],\ t_{rise,T} \le t < t_{\max,T} \\ T_{\infty,set} + (T_{\infty,\max} - T_{\infty,set}) \cos[\frac{\pi(t - t_{\max,T})}{2(t_{set,T} - t_{\max,T})}],\ t_{\max,T} \le t < t_{set,T} \\ T_{\infty,set} - (t - t_{set,T})\left(\frac{T_{\infty,set} - T_{\infty,0}}{(24 - t_{set,T})}\right),\ t_{set,T} \le t \le 24 \end{cases} \tag{34}$$

where $t_{rise,T}$ is the first point of the outdoor temperature curve; $t_{\max,T}$is the time at which the highest outdoor temperature occurs; $t_{set,T}$ is the final point of the outdoor temperature curve; $T_{\infty,0}$is the outdoor temperature at midnight; $T_{\infty,rise}$is the outdoor temperature at $t_{rise,T}$; $T_{\infty,\max}$is the maximum outdoor temperature; and $T_{\infty,set}$is the outdoor temperature at $t_{set,T}$.

In addition, the indoor temperature is maintained at $T_{\infty,i,ref}$ between $t_{rise,T}$and $t_{set,T}$with indoor air-conditioning. During time intervals without air-conditioning, the indoor and outdoor temperatures are the assumed to be the same, as given below:

$$T_{\infty,i}(t) = \begin{cases} T_{\infty,o},\ 0 \le t < t_{rise,T} \\ T_{\infty,i,ref},\ t_{rise,T} \le t < t_{set,T} \\ T_{\infty,o},\ t_{set,T} \le t \le 24 \end{cases} \tag{35}$$

where the reference temperature difference ΔT_{ref} is defined by

$$\Delta T_{ref} = \frac{G_{s,o}}{k_m/H} \tag{36}$$

To simplify the numerical model, all dimensional equations are converted to dimensionless equations.

2.4. Calculations of thermal and electrical physical parameters

(a) Average temperature of the PV cell surface

$$T_{pv,avg} = \frac{1}{H}\int_0^H T_{pv}dy \tag{37}$$

(b) Average electrical generation efficiency of the PV cell surface

The average electric generating efficiency of the PV cell surface ($\eta_{pv,avg}$) is obtained by integrating the local electrical generation efficiency over the y-axis.

$$\eta_{pv,avg} = \frac{1}{H}\int_0^H \eta_{pv}dy^+ = \int_0^1 \eta_{pv}dy \tag{38}$$

(c) Total electric generating capacity of the PV cell in the time domain

The total electric generating capacity of the PV cell is obtained by integrating each time interval over the y-axis.

$$Q_{pv,E}(\Delta t) = \int_{t_{rise}}^{t_{rise}+\Delta t}\int_0^H \dot{E}_{pv}dy^+dt = \int_{t_{rise}}^{t_{rise}+\Delta t}\int_0^H G_s\eta_{pv}dy^+dt = \int_{t_{rise}}^{t_{rise}+\Delta t} G_sH\eta_{pv,avg}dt \tag{39}$$

(d) Time averaged electric-generating efficiency of the PV cell

The average electric-generating efficiency of the surface of the PV cell during the day will fluctuate with changes in the average surface temperature. Therefore, the ratio of the electricity generated within the time interval to the overall solar radiation ($\bar{\eta}_{pv,avg}$) is needed to compare the performance of the PV cell at different time intervals.

$$\bar{\eta}_{pv,avg}(\Delta t) = \frac{Q_{pv,E}(\Delta t)}{Q_s(\Delta t)} = \frac{\int_{t_{rise}}^{t_{rise}+\Delta t} G_s\eta_{pv,avg}dt}{\int_{t_{rise}}^{t_{rise}+\Delta t} G_sdt} \tag{40}$$

(e) Average surface heat transfer rate from the PV cell to the left frame wall

$$q''_{pv,in,avg} = \frac{1}{H}\int_0^H q''_{pv,in}dy^+ \tag{41}$$

(f) Total heat transferred from the PV cell to the left frame wall in the respective time interval

$$Q_{pt,Left,o}(\Delta t) = H\int_t^{t+\Delta t} q''_{pv,in,avg}dt \tag{42}$$

(g) Average surface heat transfer rate from the left frame wall to the MEPCM layer

$$q''_{pt,Left,i,avg} = \frac{1}{H}\int_0^H q''_{pt,Left,i}dy^+ \tag{43}$$

(h) Total heat transferred from the left frame wall to the MEPCM layer in the respective time interval

$$Q_{m,o}(\Delta t) = H\int_t^{t+\Delta t} q''_{pt,Left,i,avg}dt \tag{44}$$

(i) Average surface heat transfer rate from the MEPCM layer to the right frame wall

$$q''_{pt,Right,o,avg} = \frac{1}{H}\int_0^H q''_{pt,Right,o}dy^+ \tag{45}$$

(j) Total heat transmitted from the MEPCM layer to the right frame wall in the respective time interval

$$Q_{m,i}(\Delta t) = H\int_t^{t+\Delta t}\int_0^H q''_{pt,Right,o}dy^+dt \tag{46}$$

(k) Average surface heat transfer rate transmitted from the right frame wall to the internal environment

$$q''_{pt,Right,i,avg} = \frac{1}{H}\int_0^H q''_{pt,Right,i}dy^+ \tag{47}$$

(l) Total heat transmitted from the right frame wall to the internal environment in the respective time interval

$$Q_{pt,Right,i}(\Delta t) = \int_t^{t+\Delta t}\int_0^H q''_{pt,Right,i}dy^+dt \tag{48}$$

(m) Energy fraction stored by the MEPCM layer in the respective time interval

Assuming that the direction of heat transfer is positive from left to right, there are four cases that correspond to heat entering and exiting the inner and outer walls of the MEPCM layers. The range of $Q^*_{m,stored}$ is between 0 and 1,where 0 corresponds to the case in which both the inner and outer walls of the MEPCM layer dissipate the heat and 1 corresponds to the case in which there is heat input to both the inner and outer walls of the MEPCM layer.

(1) $Q_{m,o} > 0 \& Q_{m,i} > 0$:

$$\Rightarrow Q_{PCM,in} = Q_{m,o};\quad Q_{PCM,out} = Q_{m,i}$$
$$\Rightarrow Q^*_{m,stored}(\Delta t) = 1 - \frac{Q_{PCM,out}}{Q_{PCM,in}} \tag{49}$$

Table 1
Summer environmental parameters.

U_o (W/m² K)	12	$t_{rise,T}$ (h)	6
$U_{i,on}$ (W/m² K)	10	$t_{max,T}$ (h)	14
$U_{i,off}$ (W/m² K)	5	$t_{set,T}$ (h)	19
$G_{s,o}$ (W/m²)	800	$T_{\infty,night}$ (°C)	25.9
$t_{rise,Gs}$ (h)	6	$T_{\infty,rise}$ (°C)	24.3
$t_{max,Gs}$ (h)	14	$T_{\infty,max}$ (°C)	32.3
$t_{set,Gs}$ (h)	19	$T_{\infty,set}$ (°C)	28.1

Table 2
Geometric parameters.

H	5 cm
W	To be determined (cm)
δ_{pv}	1.8 mm
H_{pt}	1.8 mm
W_{pt}	2 mm
d_p^+	18 μm

Table 3
Physical parameters.

k_m	0.41 W/m K	$c_{p,p}$	1800 J/kg s
k_{pv}	168 W/m K	$c_{p,pv}$	2790 J/kg s
k_f	0.613 W/m K	$c_{p,pt}$	900 J/kg s
k_{pt}	237 W/m K	$c_{p,g}$	750 J/kg s
h_{ls}	172000 J/kg	α_f	1.47×10^{-7} m²/s
μ_f	8.55×10^{-4} kg/m s	$\alpha_{r,pv}$	0.45
ν_f	8.575×10^{-7} m²/s	$\beta_{T,f}$	276.1×10^{-6} 1/K
ρ_f	997.1 kg/m³	κ_{pv}	4.5×10^{-3}%/K
ρ_p	900 kg/m³	ϕ_f	0.46
ρ_{pv}	883 kg/m³	$\eta_{pv,ref}$	0.2
ρ_{pt}	2700 kg/m³	C_F	0.55
ρ_g	2500 kg/m³	$T_{pv,ref}$	25 °C
$c_{p,f}$	4179 J/kg s	$T_{\infty,i,ref}$	25 °C

(2) $Q_{m,o} > 0$ & $Q_{m,i} < 0$:

$$\Rightarrow Q_{PCM,in} = Q_{m,o} + Q_{m,i}; \quad Q_{PCM,out} = 0$$
$$Q^*_{m,stored}(\Delta t) = 1 - \frac{Q_{PCM,out}}{Q_{PCM,in}} = 1 \tag{50}$$

(3) $Q_{m,o} < 0$ & $Q_{m,i} < 0$:

$$\Rightarrow Q_{PCM,in} = Q_{m,i}; \quad Q_{PCM,out} = Q_{m,o} \Rightarrow Q^*_{m,stored}(\Delta t) = 1 - \frac{Q_{PCM,out}}{Q_{PCM,in}} \tag{51}$$

(4) $Q_{m,o} < 0$ *and* $Q_{m,i} > 0$:

$$\Rightarrow Q_{PCM,in} = 0; \; Q_{PCM,out} = Q_{m,o} + Q_{m,i} \Rightarrow Q^*_{m,stored}(\Delta t) = 0 \tag{52}$$

2.5. Parameter setting

This study mainly focuses on the impact of the thickness and the melting point of the PCM in the MEPCM on the capacity for electric generation and temperature control of the PV/MEPCM module. Under summer conditions, the total indoor thermal convection coefficient is divided into a period with indoor air-conditioning ($U_{i,on}$) and a period without indoor air-conditioning ($U_{i,off}$); the fluid in the MEPCM layer is water, and the frame wall is made of copper. The values of various parameters are given in Tables 1–3.

2.6. Numerical methods

A variable density grid system is used to improve the resolution of the numerical method. The time, space, convection, and vorticity wall boundary terms are treated by the first-order backward, second-order central, FOU scheme, and Thom formula discretizations, respectively. Implicit schemes are employed for the temporal discretization. There are two loops in the numerical simulation calculation process: the time loop and the space loop. The iterative calculation continued until a prescribed relative convergence of 10^{-5} was satisfied for all the field variables in this problem.

Table 4
Set of simulation parameters for model vilification.

U_o (W/m² K)	4.36	$t_{rise,T}$ (h)	6
$U_{i,on}$ (W/m² K)	3	$t_{max,T}$ (h)	14
$U_{i,off}$ (W/m² K)	2.8	$t_{set,T}$ (h)	19
$G_{s,o}$ (W/m²)	250	$T_{\infty,night}$ (°C)	18.5
$t_{rise,Gs}$ (h)	6	$T_{\infty,rise}$ (°C)	17.7
$t_{max,Gs}$ (h)	15	$T_{\infty,max}$ (°C)	24.2
$t_{set,Gs}$ (h)	19	$T_{\infty,set}$ (°C)	20.6

3. Results and discussion

3.1. Comparison of the simulation and experimental results

The numerical simulation was first performed using experimental data from April 2011 for the average daily amount of sunlight, outdoor temperature, and outdoor wind speed. The simulated results were compared to the measured average surface temperature of the PV module. The overall heat convection coefficient in the indoor and outdoor environment was estimated using $U_o = 2.8 + 3V_w$, where V_w is the wind speed. The average measured wind speed was 0.52 m/s; therefore, the outdoor overall heat convection coefficient used in the simulation was 4.36 W/m² K. The values of the other environmental parameters used in the simulations are shown in Table 4. The amount of solar radiation and the variation in the outdoor ambient temperature are shown in Fig. 4.

Fig. 5 shows that our predictions for the surface temperature of the PV cell were generally in agreement with the experimental data. Because the solar radiation values used in the simulation were slightly higher than the experimental values, the simulated temperature of the PV cell was slightly higher than that given by the experimental data. The simulation results showed that the solar radiation increased over time after sunrise, resulting in an increase in the temperature of the PV cell. Because there is no solar radiation after sunset, the PV cell temperature was mainly controlled by the

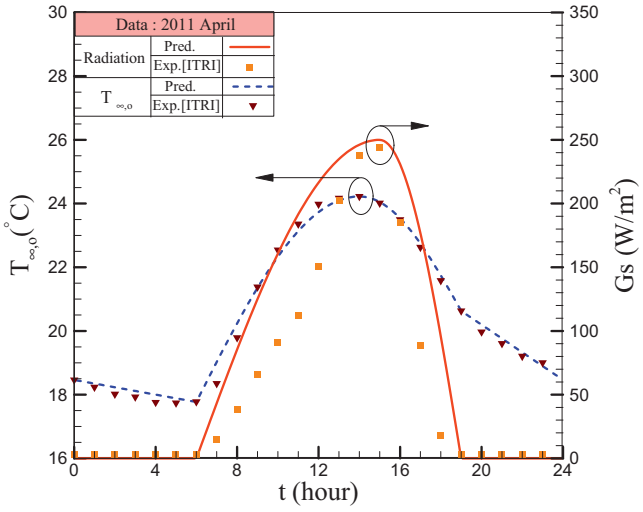

Fig. 4. The solar radiation and outdoor temperature used in this stage simulation works.

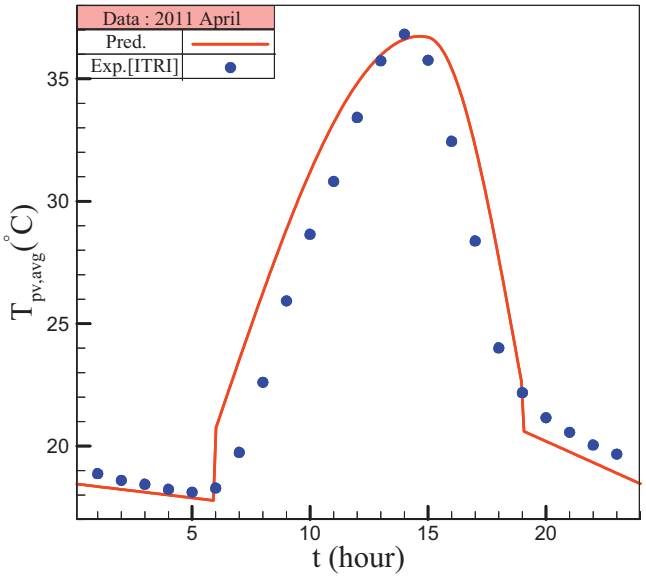

Fig. 5. Comparison of simulation results and experimental data.

outdoor environmental temperature and fell rapidly to the same level as the outdoor ambient temperature.

3.2. Effect of the MEPCM melting point

In the summer, outdoor air temperatures are high, and there is strong sunshine; thus, the temperature of the PV cell should highly increase. If the selected melting point of the MEPCM layer is too low, the MEPCM layer cannot afford to absorb latent heat during peak sunshine hours to maintain the PV cell temperature, resulting in a high PV cell temperature, which in turn causes the electric generation efficiency to decrease significantly. Moreover, the MEPCM layer cannot solidify completely, even during the nocturnal cooling period, and thus, the phase change cycle cannot be recovered completely. As a result, the full effect of the latent heat absorption cannot be repeatedly exploited by the MEPCM layer, which therefore loses its effectiveness. The simulation results for the temperature of the untreated PV module in the summer showed that the melting points for the phase change were 26 °C, 30 °C, and 32 °C for a 2-cm-thick MEPCM layer.

Fig. 6 shows the simulation results for PV/MEPCM cells with melting points of 26 °C and 30 °C compared to those for the untreated PV cell under summer conditions. The figure shows that

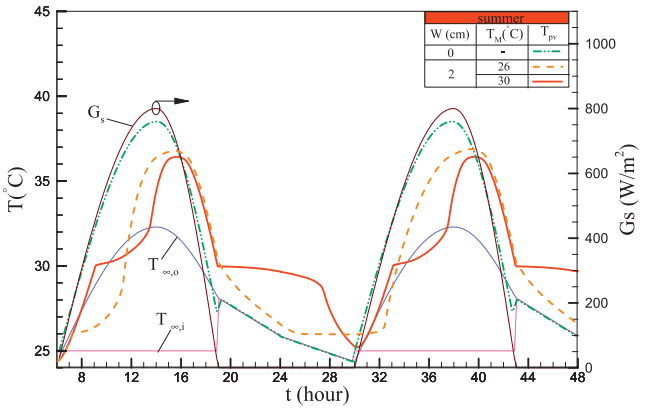

Fig. 6. Average surface temperature of the untreated PV cell and the PV/MEPCM cells with PCM melting points of 26 °C and 30 °C.

the 26 °C-melting-point MEPCM layer began to melt at 7:30 am and was completely melted by 12:00 pm; the temperature of the PV/MEPCM cell then rapidly increased and reached a maximum temperature of 36.8 °C at 3:30 pm, after which the temperature began to decline. The liquid phase of the MEPCM layer continued to solidify until approximately 1:20 am the next day. Because the outdoor temperature in the summer is relatively high (higher than 26 °C most of the time), there was insufficient time for the MEPCM layer to solidify. Consequently, before the MEPCM completely solidified, the MEPCM layer began to receive solar radiation on the next day. The outdoor temperature began to increase again, and the MEPCM layer began to melt instead of solidifying. Because only a small amount of solidification occurred during the night, a limited amount of latent heat was absorbed, and the MEPCM layer melted completely in a very short time period. However, even with the loss of the latent heat absorption effect, the heat transferred into the PV cell can still be transferred to the indoor environment via the MEPCM frame walls, and a portion of the heat can also be absorbed due to the sensible heat of the MEPCM layer. Therefore, the maximum temperature of the PV/MEPCM cell reached 36.9 °C on the second day, which was still lower than the maximum temperature of the untreated PV cell. Thus, the results indicate that an MEPCM layer with a melting point of 26 °C is not effective under summer climatic conditions.

The PV/MEPCM cell with a PCM melting point of 30 °C reached the melting temperature at 9:00 am, followed by melting of the layer, which was accompanied by a continued increase in the temperature of the PV/MEPCM cell due to the strong intensity of the summer solar radiation. However, there was already a significant temperature difference between the PV/MEPCM cell and the untreated PV cell. The MEPCM layer melted completely at 1:30 pm, followed by a rapid increase in the PV cell temperature up to a maximum temperature of 36.4 °C at 3:40 pm. The PV/MEPCM cell with a PCM melting point of 30 °C exhibited a maximum temperature that was 0.2 °C lower and occurred approximately 10 min later than the maximum temperature for the 26 °C layer. The temperature of the PV/MEPCM cell began to decline beyond the maximum temperature. The MEPCM layer started to solidify at 7:00 pm and completely solidified at approximately 3:30 am the next morning. Meanwhile, the temperature of the PV/MEPCM cell continued to decline until sunrise on the next day. The temperature of the PV/MEPCM cell then began to increase again as the solar radiation and outdoor temperature increased. Due to the complete solidification of the MEPCM layer during the nocturnal cooling period, the phase change cycle was completed. In the daytime on the second day, the MEPCM layer exploited the full effect of the latent heat absorption. Consequently, the temperature variation of the PV/MEPCM cell on the next day was consistent with the first day, exhibiting the same trend. The melting situation of the MEPCM layer at a different time is shown in Fig. 7.

For comparison with the 30 °C melting point MEPCM layer, we further increased the melting point of the MEPCM layer to 32 °C. The results are shown in Fig. 8. The PV/MEPCM cell with a melting point of 32 °C reached the melting temperature at 10:00 am, when the MEPCM layer began to melt. The layer completely melted at approximately 3:00 pm; in the meantime, the temperature of the PV/MEPCM cell started to increase, reaching a maximum of 35.3 °C at 4:15 pm, which was 1.1 °C lower than the maximum temperature attained for the MEPCM layer with a melting point of 30 °C. The maximum temperature occurred 35 minutes later than for the MEPCM layer with a melting point of 30 °C. The temperature of the PV/MEPCM cell subsequently started to decline until the phase change temperature was reached at approximately 6:20 pm, at which point the MEPCM layer began to solidify, completing the phase change cycle at 0:15 am the next day.

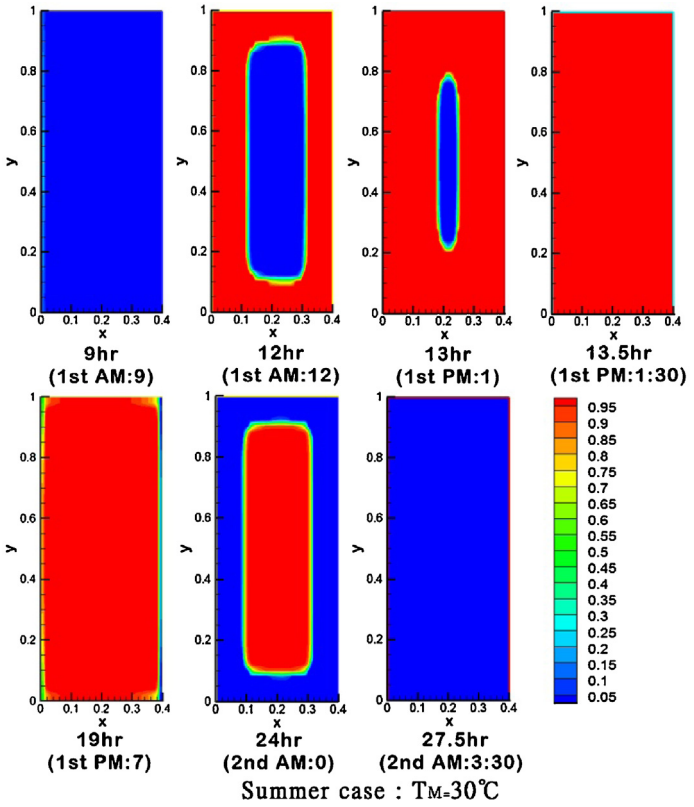

Fig. 7. Variation in the melting situation over the PV/MEPCM cell (30 °C melting point and 2-cm MEPCM layer thickness).

3.3. *Effect of the MEPCM layer thickness*

The PV/MEPCM cell module may not reach as high a temperature in the spring and fall as in the summer; in addition, the time period over which the temperature remains above 32 °C might not be as long in the spring and fall as in the summer. Thus, a MEPCM layer with a melting point of 32 °C may not be effective in the spring and autumn. Therefore, a MEPCM layer with a melting point of 30 °C was used to investigate the effect of the MEPCM layer thickness. The layer thickness was increased from 2 cm (A_m = 0.4) to 3 cm (A_m = 0.6) to explore the effect of layer thickness on the PV/MEPCM cell temperature.

Fig. 9 shows that the PV/MEPCM cell with a 3-cm-thick MEPCM layer did not melt completely at the sunshine peak (2:00 pm).

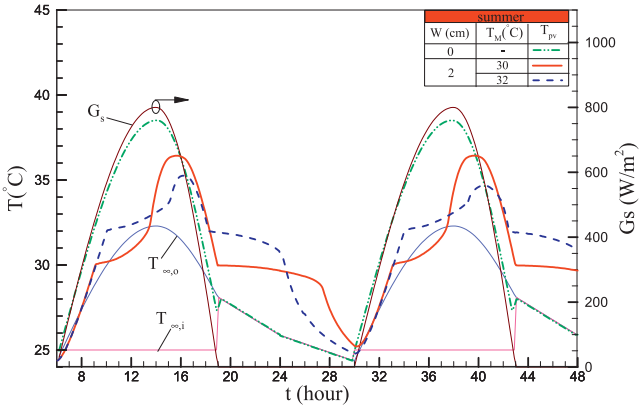

Fig. 8. Average surface temperatures of an untreated PV cell and PV/MEPCM cells with MEPCM layer melting points of 30 °C and 32 °C.

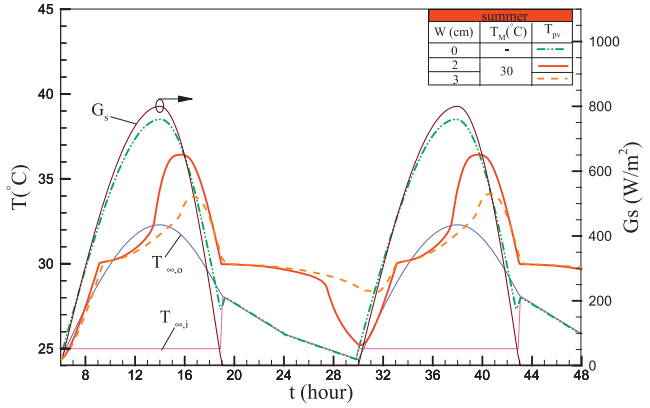

Fig. 9. Average surface temperatures for the untreated PV cell and the PV/MEPCM cell with various MEPCM layer thicknesses.

Therefore, the increase in the temperature of the PV/MEPCM cell could be controlled using latent heat absorption. Subsequently, the solar radiation began to decline, but because the solar radiation and the outdoor temperature were still relatively high, the MEPCM layer continued to melt, and the absorbed external heat was transferred into the system between 2:00 pm and 3:00 pm. At approximately 3:30 pm, the MEPCM layer melted completely, and the temperature of the PV/MEPCM cell continued to increase. However, because the sunshine radiation and outdoor temperature had declined, the increase in the temperature of the PV/MEPCM cell was not significant. The maximum temperature reached 33.9 °C at 4:40 pm.

Increasing the layer thickness increases the MEPCM content of the PV cell; therefore, a longer time is required for complete solidification during the cooling period. The figure shows that the MEPCM layer began to solidify at 7:00 pm. The temperature of the PV/MEPCM cell was maintained at approximately the melting temperature throughout the entire subsequent evening period. The MEPCM layer did not completely solidify until 7:00 am the next day. At this time, the solar radiation and outdoor temperature began to increase, along with the temperature of the PV/MEPCM cell, which reached the melting temperature again at 9:00 am the next morning. As a result, the MEPCM layer began to melt, effectively controlling the increase in the temperature of the PV/MEPCM cell again. The variation in the temperature profile for the PV/MEPCM cell throughout the next day was the same as the temperature variation during the first day. These simulation results confirmed that a 3-cm-thick MEPCM layer with a melting point of 30 °C can still complete the phase change cycle under summer conditions and that the latent heat absorption effect can be repeatedly exploited to control the temperature increase of the PV/MEPCM cell. In addition, melting can continue even during peak sunshine hours (from 1:00 pm to 3:00 pm), preventing the electric generation efficiency from substantially decreasing due to the high cell temperature caused by strong sunshine. Therefore, a melting point at 30 °C and a 3-cm thickness for a MEPCM layer is an effective combination under summer conditions.

3.4. *Thermal management capabilities*

Fig. 10 shows the energy storage fraction and the total heat transfer for a PV/MEPCM cell with a melting point of 30 °C and a thickness of 2 cm. These curves are similar to those for a PV/MEPCM cell with a melting point of 32 °C and a thickness of 2 cm and the PV/MEPCM cell with a melting point of 30 °C and a thickness of 3 cm; therefore, these two PV/MEPCM cells will not be discussed in this paper. The initial system temperature for the calculations

Table 5
Overall performance of untreated PV cells versus PV/MEPCM cells.

Summer	W (cm)	T_M (°C)	$T_{pv,max}$ (°C)	$\eta_{pv,min}$ (%)	$\eta_{pv,min}$ increase (%)	$\eta_{pv,day}$ (%)	$\eta_{pv,day}$ increase (%)	$Q_{pv,E,day}$ (%)	$Q_{pv,E,day}$ increase (%)
PV cell Without MEPCM	0	–	38.5	18.784	–	19.040	–	226.873	–
PV/MEPCM cell	2	32	35.3[II]	19.077[II]	1.560	19.328[II]	1.513	230.305[II]	1.513
	2	30	36.4[II]	18.971[II]	0.996	19.327[II]	1.507	230.316[II]	1.518
	3	30	34.1[II]	19.179[II]	2.103	19.422[II]	2.006	231.439[II]	2.013

[II] Second day data.

was set to 24.3 °C, which corresponded to the outdoor temperature at 6:00 am. The outdoor temperature immediately increased, and the indoor temperature was 25 °C at the start of the simulation. Thus, the MEPCM layer absorbed heat from both the indoor and outdoor environment, resulting in an initial energy storage fraction of unity. The system temperature then gradually increased by absorbing heat. When the system temperature was higher than the indoor room temperature, the heat in the system began to be discharged to the indoor environment, causing the energy storage fraction to gradually decrease as the system temperature increased.

Fig. 10 shows that the system temperature was maintained at the phase change temperature when the MEPCM layer began to melt, causing the total heat transfer ($Q_{m,i}$) to increase slowly. At the same time, the heat transferred into the system from the outdoor environment continued to increase, and the energy storage fraction increased accordingly. When the MEPCM layer melted completely, the rate of the increase in the total heat transfer to the inner wall of the layer increased. The energy storage fraction began to decline. The energy storage fraction change on the second day showed the same trend as the solar radiation curve. The heat absorbed by the MEPCM layer from outside increased as the solar radiation and outdoor temperature gradually increased over the morning period. Therefore, the energy storage fraction showed an increasing trend. However, after the peak sunshine period, the heat absorbed by the MEPCM layer from solar radiation gradually decreased. At the same time, the heat exhaust from the MEPCM layer increased due to the large temperature difference between the MEPCM layer and the external temperature. As a result, the energy storage rate began to decline.

Fig. 11 shows the total heat transfer that entered and exited the outer and inner walls of the MEPCM layer. The total heat transfer of inner wall for the MEPCM layer (30 °C melting point, 2 cm thickness) was significantly lower than the other two sets of data after 2:00 pm; however, the total heat transfer of the outer wall was higher than the other two sets of data, indicating that this MEPCM layer (30 °C melting point, 2 cm thickness) had a superior energy storage fraction.

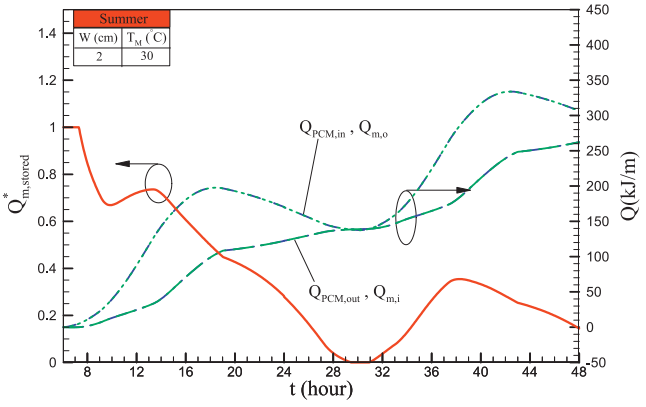

Fig. 10. Energy storage fraction and total heat transfer for the PV/MEPCM cell with a melting point of 30 °C and a thickness of 2 cm.

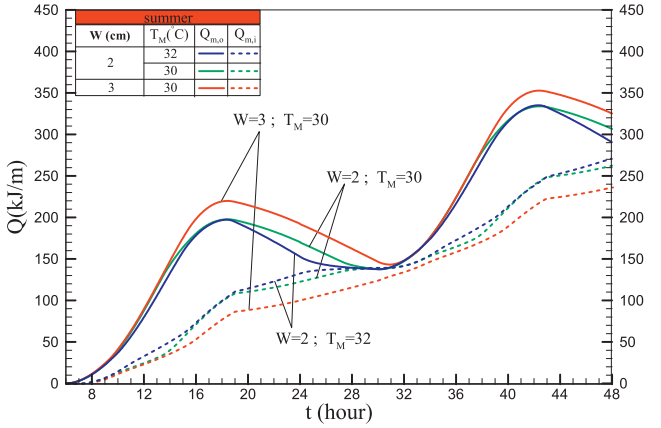

Fig. 11. Total heat transfer entering and exiting the inner and outer walls of the PV/MEPCM cell.

3.5. Comparison of thermal/electrical performance

Table 5 shows the performance of the untreated PV cell and the PV/MEPCM cells under different conditions. It is obvious that an MEPCM layer can be used as a passive temperature control device to improve the performance of a PV cell. The PV/MEPCM cell with 30 °C melting point and 3 cm layer thickness showed the best performance. The maximum surface temperature of the PV/MEPCM cell (30 °C melting point, 3 cm layer thickness) was 34.1 °C, 4.4 °C lower than that for untreated PV cell. The average minimum electric generation efficiency and the single-day time-averaged electric generation efficiency of this PV/MEPCM cell were 19.179% and19.422%, respectively, an increase of 2.103% and 2.006%, respectively, over the corresponding efficiencies for the untreated PV cell. The single-day total electrical generating capacity was 231.439 kJ/m, a 2.013% increase over the untreated PV cell capacity. The PV/MEPCM cell with a melting point of 32 °C and a 2 cm layer thickness also exhibited a relatively high minimum average electrical generation efficiency because the maximum surface temperature was lower than that of the PV/MEPCM cell with a 30 °C melting point and 2-cm layer thickness. However, in terms of the single-day time averaged electric generation efficiency and the single-day total electric generation, there was no difference between the PV/MEPCM cell with a 2-cm layer thickness and a 30 °C melting point and that with a 32 °C melting point.

4. Conclusion

This study investigated the impact of MEPCM layers on the surface temperature, electric generation efficiency and electric generation capacity of PV cells under different environmental conditions. The analysis of the simulation results yielded recommendations for optimal melting points and layer thicknesses for a PV module integrated with a MEPCM under summer conditions. The conclusions of the study are summarized below.

In this study, the simulation results for the PV cell heat transfer, outdoor temperature curve and solar radiation curve generally agree with the experimental data.

In winter, the untreated PV cell had a maximum average surface temperature of 26.7 °C, a minimum surface average electric generation efficiency of 19.846%, and a single-day total electric generation capacity of 100.435 kJ/m; in summer, the highest average surface temperature was 38.5 °C, the lowest average surface electric generation efficiency was 18.784%, and the single-day total electric generating capacity was 226.815 kJ/m.

Under high summer temperatures, a PV/MEPCM cell with a melting point of 30 °C and a 3-cm thickness continued to undergo a phase change during peak sunshine hours, which prevented a significant decrease in the electric generation efficiency. The maximum temperature also decreased and occurred later in time. During the nocturnal cooling period, the MEPCM layer could complete a phase change cycle, repeatedly exploiting the effect of latent heat absorption. The highest average surface temperature of the PV/MEPCM cell was 34.1 °C at 4:35 pm on the second day. The single-day total electric generating capacity reached 231.439 kJ/m, which represented an increase of 2.013% over the untreated PV cell value.

The modeling and simulation results are limited to the used core material (pure PCM compound, paraffin) and the chosen specific location. To explore the practical aspect and applications at other locations, PCMs with wide melting range and different melting point could be tested. The model validation was based on the no PCM case, more detailed weather conditions and physical prototyping works are definitely needed, which are necessary steps towards developing more reliable predictive tools for system design of a BIPV module integrated with a MEPCM layer.

References

[1] M.E. Meral, F. Dinçer, A review of the factors affecting operation and efficiency of photovoltaic based electricity generation systems, Renewable and Sustainable Energy Reviews 15 (2011) 2176–2184.

[2] J. Zuo, W. Li, L. Weng, Thermal performance of caprylic acid/1-dodecanol eutectic mixture as phase change material (PCM), Energy and Buildings 43 (1) (2011) 207–210.

[3] S. Wu, G. Fang, Dynamic performances of solar heat storage system with packed bed using myristic acid as phase change material, Energy and Buildings 43 (5) (2011) 1091–1096.

[4] A. Waqas, S. Kumar, Thermal performance of latent heat storage for free cooling of buildings in a dry and hot climate: an experimental study, Energy and Buildings 43 (10) (2011) 2621–2630.

[5] J. Koo, H. So, S.W. Hong, H. Hong, Effects of wallboard design parameters on the thermal storage in buildings, Energy and Buildings 43 (8) (2011) 1947–1951.

[6] I. Ceron, J. Neila, M. Khayet, Experimental tile with phase change materials (PCM) for building use, Energy and Buildings 43 (8) (2011) 1869–1874.

[7] A.L.S. Chan, Energy and environmental performance of building facades integrated with phase change material in subtropical Hong Kong, Energy and Buildings 43 (10) (2011) 2947–2955.

[8] C.M. Lai, R.H. Chen, C.Y. Lin, Heat transfer and thermal storage behaviour of gypsum boards incorporating micro-encapsulated PCM, Energy and Buildings 42 (8) (2010) 1259–1266.

[9] C. Hasse, M. Grenet, A. Bontemps, R. Dendievel, H. Sallee, Realization, test and modelling of honeycomb wallboards containing a phase change material, Energy and Buildings 43 (1) (2011) 232–238.

[10] A. Karaipekli, A. Sari, Preparation and characterization of fatty acid ester/building material composites for thermal energy storage in buildings, Energy and Buildings 43 (8) (2011) 1952–1959.

[11] R. Zeng, X. Wang, H. Di, F. Jiang, Y. Zhang, New concepts and approach for developing energy efficient buildings: ideal specific heat for building internal thermal mass, Energy and Buildings 43 (5) (2011) 1081–1090.

[12] B.M. Diaconu, Thermal energy savings in buildings with PCM-enhanced envelope: Influence of occupancy pattern and ventilation, Energy and Buildings 43 (1) (2011) 101–107.

[13] R. Ansuini, R. Larghetti, A. Giretti, M. Lemma, Radiant floors integrated with PCM for indoor temperature control, Energy and Buildings 43 (11) (2011) 3019–3026.

[14] F. Berroug, E.K. Lakhal, M. El Omari, M. Faraji, H. El Qarnia, Thermal performance of a greenhouse with a phase change material north wall, Energy and Buildings 43 (11) (2011) 3027–3035.

[15] P. Arce, C. Castellon, A. Castell, L.F. Cabeza, Use of microencapsulated PCM in buildings and the effect of adding awnings, Energy and Buildings 44 (2012) 88–93.

[16] C.J. Ho, A.O. Tanuwijava, Chi-Ming Lai, Thermal and electrical performance of a BIPV integrated with a microencapsulated phase change material layer, Energy and Buildings 50C (2012) 331–338.

[17] M.J. Huang, P.C. Eames, B. Norton, Phase change materials for limiting temperature rise in building integrated photovoltaics, Solar Energy 80 (2006) 1121–1130.

[18] S. Maiti, S. Banerjee, K. Vyas, P. Patel, P.K. Ghosh, Self regulation of photovoltaic module temperature in V-trough using a metal–wax composite phase change matrix, Solar Energy 85 (9) (2011) 1805–1816.

[19] R. Baetens, B.P. Jelle, A. Gustavsen, Phase change materials for building applications: a state-of-the art review, Energy and Buildings 42 (2010) 1361–1368.

[20] F. Kuznik, D. David, K. Johannes, J.J. Roux, A review on phase change materials integrated in building walls, Renewable and Sustainable Energy Reviews 15 (1) (2011) 379–391.

[21] L.F. Cabeza, A. Castell, C. Barreneche, A. de Gracia, A.I. Fernandez, Materials used as PCM in thermal energy storage in buildings: a review, Renewable and Sustainable Energy Reviews 15 (3) (2011) 1675–1695.

[22] V.V. Tyagi, S.C. Kaushik, S.K. Tyagi, T. Akiyama, Development of phase change materials based microencapsulated technology for buildings: a review, Renewable and Sustainable Energy Reviews 15 (2) (2011) 1373–1391.

[23] G. Lauriat, V. Prasad, Non-Darcian effects on natural convection in a vertical porous enclosure, International Communications in Heat and Mass Transfer 32 (1989) 2135–2148.

[24] C.J. Ho, A continuum model for transport phenomena in convective flow of solid–liquid phase change material suspensions, Applied Mathematical Modeling 29 (2005) 805–817.